DEFORMATION AND FAILURE BEHAVIOR OF OPEN-GRADED FRICTION COURSE AT LOW TEMPERATURES

Baoyang Yu[1,2], Zongguang Sun[1] and Lin Qi[3]

1. *College of Transportation Engineering, Dalian Maritime University, Dalian 116026, China; yubaoyang12380@126.com sun@dlmu.com*
2. *School of Transportation Engineering, Shenyang Jianzhu University, Shenyang 110168, China;*
3. *Department of Civil Engineering, Shenyang Urban Construction Institute, Shenyang 110167, China; qilin6126@126.com*

ABSTRACT

To study the deformation and failure behavior of the open-graded friction course (OGFC) before cracking at low temperatures, a four-point bending test of the trabecula was conducted, and the deformation process was monitored by the digital surface model (DSM). The distribution law of the strain field of the trabecular specimens was analyzed. The horizontal strain field gradually changed from a uniform distribution to a strain concentration area with loading. The crack initiation time, crack initiation strain, and deformation period were obtained from the strain curve. The combination of stress reconstruction and DSM makes the stress measurement of the OGFC more authentic.

KEYWORDS

Open-graded friction course (OGFC), Four-point bending test, Digital surface model (DSM), Strain field, Stress reconstruction

INTRODUCTION

The open-graded friction course (OGFC) has been popular since 1950 and has been used because of its advantages, such as strong drainage capacity, improved road surface friction, and low noise [1–2]. Compared with other types of mixtures, OGFC has a higher porosity and coarse aggregate content. However, owing to this unique structure, its spatial distribution has a significant influence on the deformation and failure behavior [3].

Low-temperature deformation and failure are common issues associated with asphalt pavements and have important impacts on the road function of the OGFC. Typically, the deformation and failure behavior of materials are evaluated as a whole by the nominal stress and strain in multiple macroscopic tests [4–5]. However, material properties are evaluated according to the assumption of isotropy; the anisotropic properties of the mixture are neglected [6–7]. In addition, the deformation process prior to failure is ignored. It is impossible to obtain the deformation of the sample surface or the concerned part. The actual strain field of materials must be obtained to understand their macroscopic behavior, irrespective of whether it is the surface of the sample or the place of interest [8]. Therefore, it is of great significance to study the deformation and failure behavior of OGFCs by considering comprehensively the anisotropy properties of materials.

The digital surface model (DSM) can realize full-field, noncontact measurements. Through the deformation measurement experiment of 0.1-500m scale, Maas et al. [9] determined that digital image correlation (DIC) can analyze deformation with a precision of 1:1000000. Kovačič et al. [10] found that the photogrammetry results also maintained high accuracy compared with the results

obtained by geodetic and hydraulic piston methods. Stewart et al. [11] found that cracks are sensitive to mesostructural features using DSM combined with macro tests. Bjorn et al. [12] found that a DIC system overcomes the shortcomings of traditional strain measuring equipment and has satisfactory accuracy compared with strain gauges. Through the failure test of concrete wall, Teo [13] studied that there is a high correlation between photogrammetry displacement and linear variable differential transformer (LVDT) displacement. Lyons et al. [14] studied the ability of DIC computer vision technology to measure in-plane deformation at temperatures as high as 650 °C.

Considering the above analysis, in this study, the deformation and failure behavior of OGFC is studied using DSM in conjunction with a four-point bending test to obtain the full-field displacement and strain information of the OGFC mixture. Additionally, we propose stress reconstruction, obtain the stress change during loading, and recognize the full-field deformation and failure behavior of the OGFC mixture.

METHODS

Gradation design of OGFC

OGFC is an open-graded asphalt mixture composed of asphalt and aggregates. Basalt was used as the coarse aggregate, alkaline machine-made sand was used as the fine aggregate, and the mineral powder was made of ground limestone. The gradation is illustrated in Figure 1.
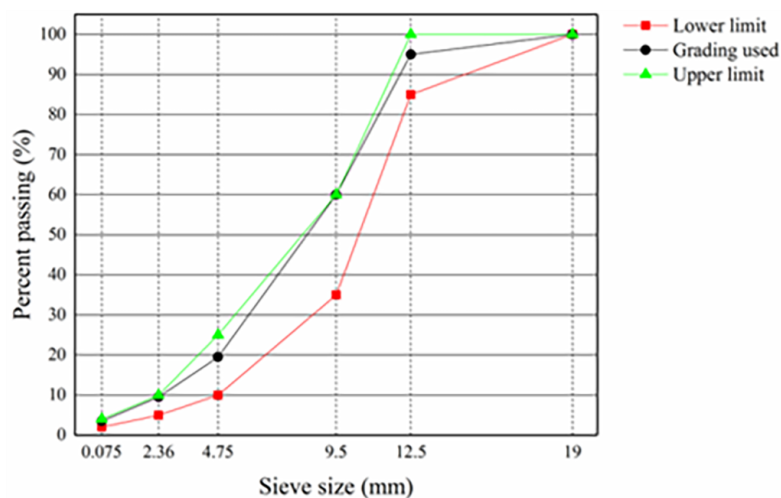

Fig. 1 – Gradation design of open-graded friction course

To verify the high-temperature stability, low-temperature crack resistance, and water stability of the OGFC, the dynamic stability was measured by conducting a rutting test at 4160 times/mm. The freeze-thaw splitting strength ratio measured by the freeze–thaw splitting test was 90.86%, and the flexural tensile strain measured by the low-temperature bending test was 3178.34 $\times 10^{-6}$.

Test methods

Basic principle of DSM

This study mainly uses the MatchID system, comprising a camera, computer, and light source, to execute the DSM test. The DSM test system is shown in Figure 2.
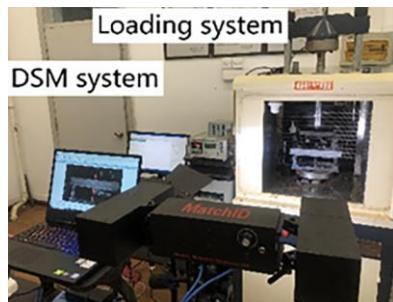
Fig. 2 – Digital speckle method test system

Basic principle of DSM [15]: Through correlation matching of speckle images before and after deformation (the images before and after deformation are reference and deformed images, respectively), the gray field of an image subregion is obtained, and the displacement and strain of sample are calculated according to the gray changes of pixel points. The algorithm principle is depicted schematically in Figure 3. The gray values of the reference and deformed images are $f(x, y)$ and $g(x', y')$, respectively. Consider a point $P(x, y)$ in the reference image, and a subset s of pixel points with a size of $(2M +1) \times (2M+1)$ as the reference image matching subarea. After loading, when point P moves to point $P'(x', y')$, the speckle in S moves to the corresponding position in the S' subregion centered on the point $P'(x', y')$. Based on the principles of probability and statistics, the deformed point P' can be determined by the position of the point with the maximum correlation coefficient after matching with point P [16]. After matching the corresponding points, the coordinate differences between these two points are the displacement components attributed to the deformation of point P [17].
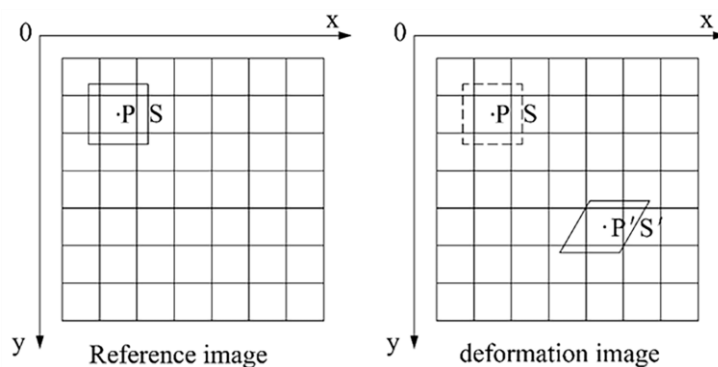

Fig. 3 – Basic principle diagram explaining the implementation of the correlation algorithm

The zero-mean normalized sum-of-squared differences (ZNSSD) correlation function [18] is used to calculate the correlation coefficient of the OGFC beam specimen before and after deformation,

$$C_{ZNNSSD} = \sum_{x=-M}^{M} \sum_{y=-M}^{M} \left[\frac{f(x,y)-f_m}{\sqrt{\sum_{x=-M}^{M}\sum_{y=-M}^{M}[f(x,y)-f_m]^2}} - \frac{g(x',y')-g_m}{\sqrt{\sum_{x=-M}^{M}\sum_{y=-M}^{M}[g(x',y')-g_m]^2}} \right] \quad (1)$$

where $f(x,y)$ is the gray value of reference image point P in Figure 3, $g(x', y')$ is the gray value of the deformed image point in Figure 3, and f_m and g_m are the average gray values of the subregions of the reference and deformed images, respectively.

___

Preparation of test pieces

The rutting plate specimen with dimensions of 300 mm × 300 mm × 50 mm (length × width × height) was cut in beam specimens with dimensions of 250 mm × 30 mm × 35 mm (length × width × height). Speckles were made on the test piece. The bottom part was sprayed with matte white paint on one side in the up-and-down direction of molding, and black spots were added after air drying to form a speckled surface with black spots on a white background, as shown in Figure 4.

Fig. 4 – Speckled surface of the tested specimen

Test scheme

The four-point bending test is shown in Figure 5. A SANS universal testing machine was used as the loading device. The distance between the supports of the specimen placement device was 200 mm, the distance between adjacent chucks was 66.67 mm, the loading rate was 50 mm/min, the test temperature was -10 °C, and the image acquisition frequency was 10 ms/pair.

Fig. 5 – Four-point bending test

ANALYSIS AND DISCUSSION OF TEST RESULTS

Load–time curve analysis

The entire field deformation and failure behavior of the OGFC were studied using DSM combined with a four-point bending test. Figure 6 illustrates the load–time curve. At the initial stage of loading, the load on the specimen increases approximately linearly. At this time, the microcracks in the specimen are gradually compressed and deformed. Subsequently, the load growth rate decreases until the peak value is reached. Finally, the load decreases approximately linearly until the end of the test. To analyze the strain field evolution process of the OGFC beam specimens before complete failure, the strain fields at six representative time points (A–F) were selected to analyze the evolution process from the load–time curve and the evolution characteristics of the strain field nephogram. Point A is the initial loading of the specimen, point B is in the stage of linear load growth, point C is in the stage of slow-load growth, point D is near the peak load, point E is at the stage of load decline, and point F is the end of the load decline when the test is terminated.
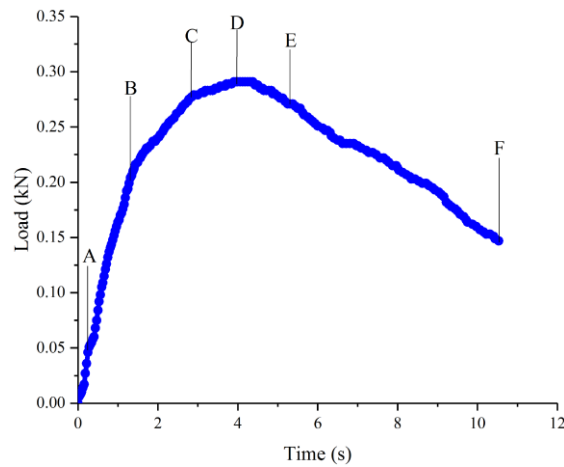
Fig. 6 – Load–time curve of four-point bending test

Strain-field evolution analysis

We focus on the evolution process of the strain field before the complete failure of the OGFC beam specimen and investigate the deformation and failure behavior by examining the evolution of the horizontal strain field [19], as shown in Figure 7(a)–(f).
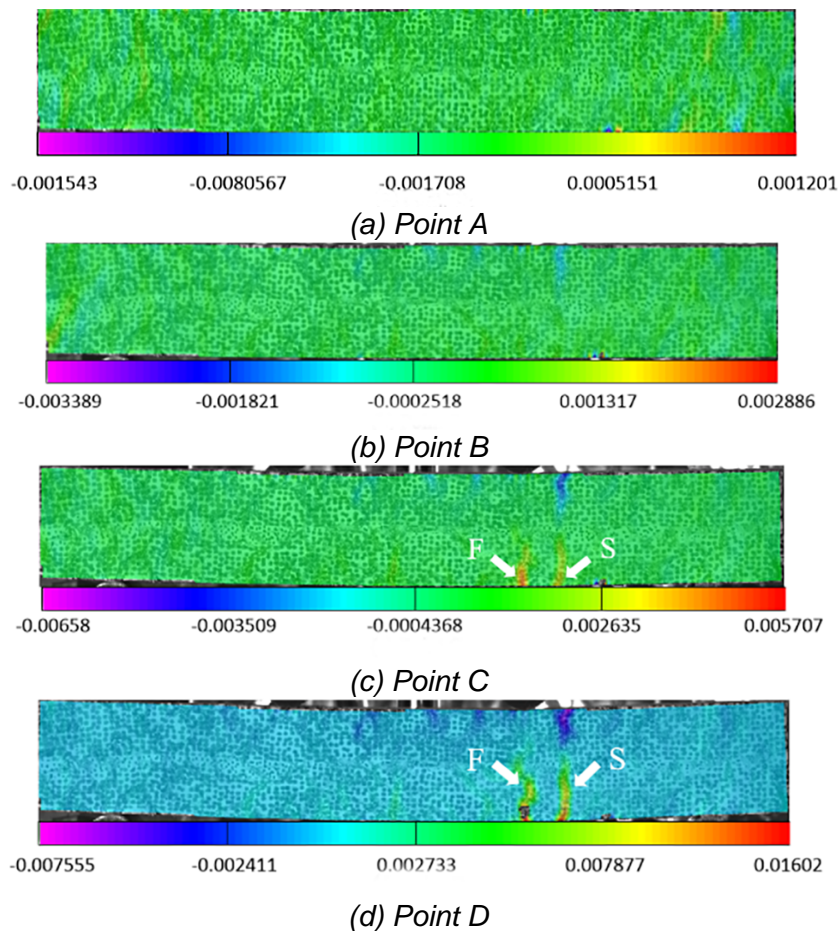

(a) Point A

(b) Point B

(c) Point C

(d) Point D

Fig. 7 – Horizontal strain field at representative temporal points
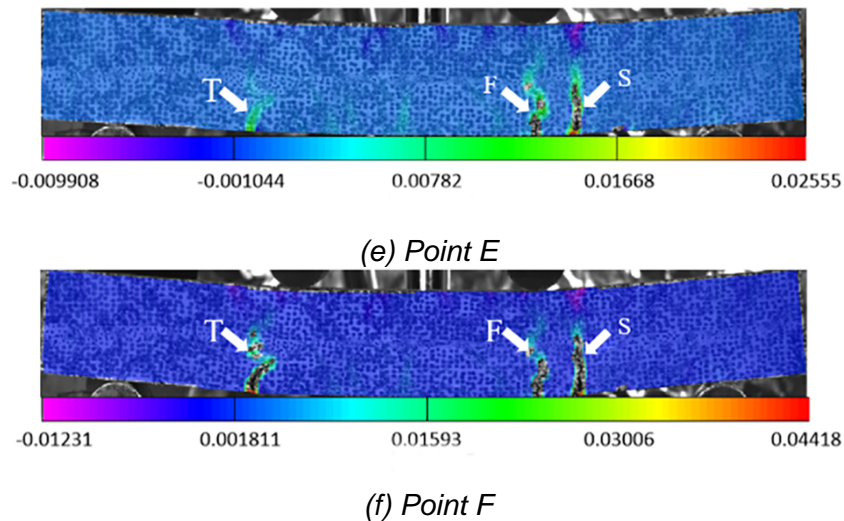
(e) Point E

(f) Point F

Fig. 7 – Horizontal strain field at representative temporal points

Figure 7 demonstrates that:

① There is no notable difference between the strain fields at points A and B, and the nephogram of the horizontal strain field is uniformly distributed; however, there is a rather fuzzy ribbon area at point B. Compared with the position of the specimen, these areas are all distributed along the asphalt mortar owing to the uneven distribution of materials, and the flexible asphalt binder is prone to deformation. Thus, different positions generate different strain responses.

② When loaded to point C, the sample is in a stage of slow load growth. First, flame-like areas F and S, namely the strain concentration areas, appear at the bottom part of the right indenter and expand upward to form the strain concentration belt area (Figure 7(c)). As indicated, the degree of strain concentration in area F is higher than that in area S. Comparing Figures 7(c) and 7(b), we can observe that areas F and S are developed from the ribbon areas in Figure 7(b).

③ When loaded at point D, the strain concentration degree of area F is higher than that of area S, and the stress is concentrated. When the concentrated stress exceeds the ultimate strength that the OGFC can bear, area F cracks before area S, as shown in Figure 7(d). Concurrently, a crack tip is produced, and the strain concentration area moves up to the tip, thus promoting continuous expansion of cracks. In addition, the first generation of cracks in area F increases the tensile strain at point D by one order of magnitude compared with point C.

④ With the application of load, the cracks in area F continue to expand, and the strain concentration in area S increases synchronously. When the material limit is exceeded, the cracks in area S appear as shown in Figure 7(e). Simultaneously, a flame-like area T appears at the bottom of the left indenter owing to the strain concentration.

⑤ The strain concentration in the left indenter and cracking in area S disperse the stress in area F and decelerate the development of cracks. When loaded to point F, the strain concentration causes the crack at the bottom of the left indenter specimen to expand to a certain extent, which in conjunction with the two cracks on the right side, leads to the final failure form of the specimen shown in Figure 7(f).

According to the overall observation of the six pairs of strain field nephograms with different characteristics at different times, the drastic changes in the strain field distribution in the four-point bending test are mainly concentrated between two indenters. The strain field gradually changes from a uniform distribution to a considerable concentration, thus indicating the localization characteristics of the OGFC deformation. In addition, by comparing the strain concentration bands to the distribution positions of the specimen materials, it can be observed that the strain concentration bands in areas F, S, and T are all located between coarse aggregates, and the

materials at the positions are asphalt mortar formed by asphalt binder and fine aggregate. Furthermore, the cracks are distributed along the asphalt mortar and spread at the interface between the fine aggregate and asphalt binder.

Strain characteristics at strain concentration zone

To objectively and quantitatively investigate the evolution of the strain concentration zone, the horizontal strain of the concerned points (1, 2, 3, and 4; Figure 8) was measured using the point function of the MatchID system, as depicted in Figure 7(c), in which three points (1, 3, and 4) were located at the cracking point of the strain concentration zone, and point 2 was located at the middle bottom. Figure 9 demonstrates the change in the horizontal strain at each point with the number of collected frames.
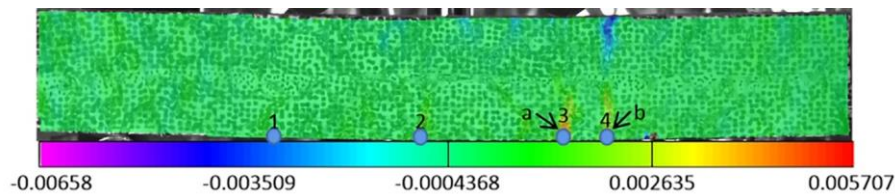

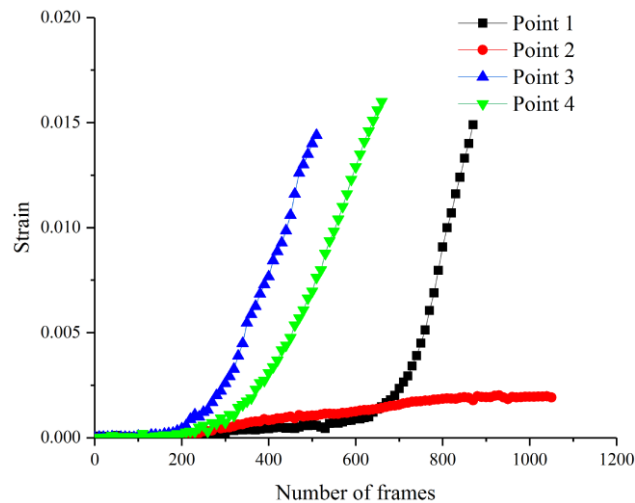*Fig. 8 – The horizontal strain of the Concerned points*

Fig. 9 – Changes of horizontal strain of concerned points with the number of frames collected

Figure 9 shows that the strain change trends of the concerned points are different, and the strain growth is slow in the early stage with no notable differences. The strain growth rate at points 3 and 4 is accelerated and tends to be linear at approximately 200 frames, but the growth rate at point 3 is faster than that at point 4 in the early stage. At approximately 600 frames at point 1, the strain begins to increase rapidly and tends to be linear. When cracks occurred at points 1, 3, and 4, the strain responses were disrupted. Considering that no cracks were formed at point 2, the curve changed steadily until the test stopped. Based on the number of frames at the turning point of the curve from slow growth to rapid growth, the cracking point sequence adheres to the order of points 3, 4, and 1, respectively. The corresponding time at the strain interruption at point 3 is the crack initiation time (4.33 s). Furthermore, the time before cracking (strain interruption) is the deformation period of the specimen, which is approximately 0–4.33 s (520 frames).
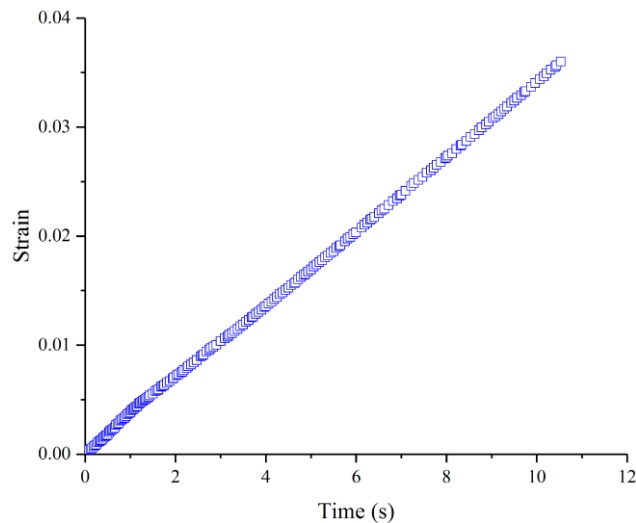
Fig. 10 – Nominal strain response of four-point bending test

The nominal strain of the four-point bending test is shown in Figure 10. Comparing Figures 9 and 10, the strain change trends present nonlinear growths and not the approximate linear growth trends of the nominal strain, although the strain change trends of the concerned points are different. This is because OGFC exhibits anisotropic properties, as verified by the distribution of the strain field and strain changes of the concerned points. The nominal strain was the ideal strain obtained by homogenizing the specimen. The DSM calculates the strain values of the points on the surface of the specimen. Therefore, the strain calculated using the DSM is the true strain value of each point.

Stress reconstruction and evolution analysis

To study the material stress variation law, a theoretical formula is generally used to calculate the stress; however, this method does not consider the change in the material's cross-section owing to load. In addition, the theoretical formula can only calculate the representative stress and cannot obtain the stress change of the concerned area or point. Previously, the stress change was studied using the finite element method (FEM) [20-21]. However, the FEM is too idealistic; thus, using DSM to estimate the stress of materials can provide more accurate results. Therefore, based on the FEM and material properties, this study reconstructs the stress of the OGFC deformation process through the stress–strain inverse mechanical analysis method based on the strain measurement results of DSM.

Stress reconstruction

The four-point bending test used in this study was performed at -10 °C. Assuming that OGFC produces elastic deformation during loading, the stress–strain relationship at the deformation stage can be expressed using Equations 2–4, according to the elastic mechanics theory as follows,

$$\varepsilon_x = \frac{1-\mu}{E}\left(\sigma_x - \frac{\mu}{1-\mu}\sigma_y\right) \tag{2}$$

$$\varepsilon_y = \frac{1-\mu}{E}\left(\sigma_y - \frac{\mu}{1-\mu}\sigma_{yx}\right) \tag{3}$$

$$\gamma_{xy} = \frac{2(1-\mu)}{E}\tau_{xy} \tag{4}$$

where σ_x is the horizontal stress, σ_y is the vertical stress, τ_{xy} is the shear stress, μ is the Poisson's ratio of the material, and E is the elastic modulus.

Assuming that $a = \frac{1-\mu}{E}$ and $b = \frac{\mu}{1-\mu}$, the above equations can be simplified to Equations 5–7, as follows,

$$\varepsilon_x = a(\sigma_x - b\sigma_y) \tag{5}$$

$$\varepsilon_y = a(\sigma_y - b\sigma_x) \tag{6}$$

$$\gamma_{xy} = 2a(1+b)\tau_{xy} \tag{7}$$

Equations 8–10 of the stress reconstructions in the horizontal, vertical, and shear directions can be obtained by the simultaneous inversion of Equations 5–7, as follows.

$$\sigma_x = \frac{\varepsilon_x - b\varepsilon_y}{a(1-b^2)} \tag{8}$$

$$\sigma_y = \frac{\varepsilon_y - b\varepsilon_x}{a(1-b^2)} \tag{9}$$

$$\tau_{xy} = \frac{1}{2a(1+b)}\gamma_{xy} \tag{10}$$

Therefore, using the elastic modulus, Poisson's ratio, and strain data, the real stress can be obtained by stress reconstruction. The elastic modulus and Poisson's ratio were calculated from the DSM in the deformation stage. The starting and ending points of the deformation stage were determined; E_{av} and μ_{av} [22] of the specimen represent the elastic modulus and Poisson's ratio, respectively.

To obtain E_{av} and μ_{av}, the line function of the MatchID analysis system was adopted, and the lines were arranged in the obtained strain nephogram. The required strain values are given by Equations 11–14, as follows,

$$\varepsilon_{ha} = \frac{1}{n}\sum_{i=1}^{n}\varepsilon_{iha} \tag{11}$$

$$\varepsilon_{ea} = \frac{1}{n}\sum_{i=1}^{n}\varepsilon_{iea} \tag{12}$$

$$\varepsilon_{hb} = \frac{1}{n}\sum_{i=1}^{n}\varepsilon_{ihb} \tag{13}$$

$$\varepsilon_{eb} = \frac{1}{n}\sum_{i=1}^{n}\varepsilon_{ieb} \tag{14}$$

where a and b are the start and end marks of the deformation stage, respectively; ε_{ha} and ε_{hb}, and ε_{ea} and ε_{eb} are the average horizontal strains and average vertical strains at the beginnings and ends of the deformation stages, respectively; n is the number of measuring points on the measuring line; ε_{iha} and ε_{ihb}, and ε_{iea} and ε_{ieb} are the horizontal and vertical strains of the measurement point i of the measuring line at the start and end points, respectively.

According to the definition of the elastic modulus and Poisson's ratio, Equations 15 and 16 are obtained as follows,

$$E_{av} = \frac{\sigma_b - \sigma_a}{\varepsilon_{hb} - \varepsilon_{ha}} \tag{15}$$

$$\mu_{av} = \frac{\varepsilon_{eb} - \varepsilon_{ea}}{\varepsilon_{hb} - \varepsilon_{ha}} \tag{16}$$

where σ_a and σ_b are the stress values at the beginning and end of the deformation stage, respectively.

Stress analysis based on DSM

As observed earlier, the elastic deformation time of the OGFC beam specimen is in the range of 0–4.33 s (0–520 frames), and its horizontal and vertical strains are both zeroes because

there is no stress at the beginning. The horizontal and vertical strains at the end of the deformation stage can be obtained by combining the corresponding relationship between time and strain. The strain field is shown in Figure 11.
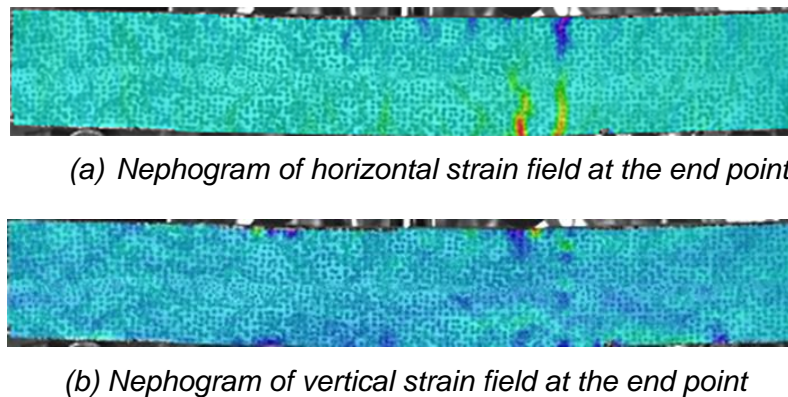

(a) Nephogram of horizontal strain field at the end point

(b) Nephogram of vertical strain field at the end point

Fig. 11 – Nephogram of horizontal strain and vertical strain fields at the end point

Based on the stress condition, a measuring line was placed horizontally along the top and bottom edges of the test surface of the specimen to calculate the average horizontal strain. Further, a measuring line was placed vertically directly below the loading end to calculate the average vertical strain. A total of 51 points from each measuring line were used to obtain the strain change of the test piece, as shown in Figure 12. In Figure 12(a), the fluctuations of the top and bottom measuring lines are located at the middle measurement point, and the fluctuation of the top measuring line is much smaller than that of the bottom. This indicates that the deformation of the test piece occurs between the loading ends. The top is the compressive strain, and the bottom is the tensile strain, which plays a major role in the deformation. In Figure 12(b), the left measuring line is parallel to the right measuring line, exhibiting no significant changes. However, compared with Figure 12(a), vertical strain value is one order of magnitude smaller than the horizontal strain value, thus indicating that the horizontal strain primarily affects the test piece. The irregular fluctuation and peak value of the measuring lines in Figures 12(a) and 12(b) demonstrate the anisotropic characteristics of the OGFC; accordingly, the applicability of DSM to OGFC is verified.
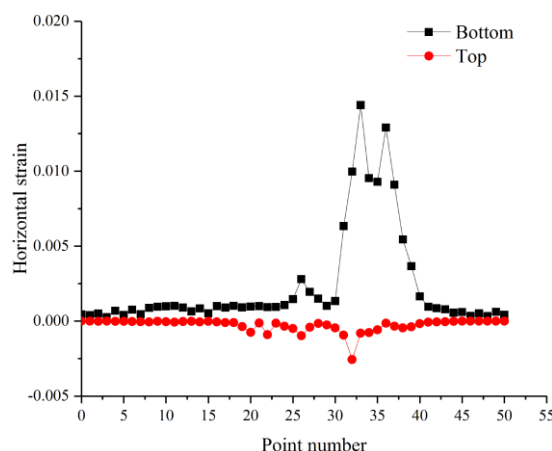
*(a) Horizontal strain of the top and bottom measuring lines*

Fig. 12 – Horizontal and vertical strains of the measuring lines
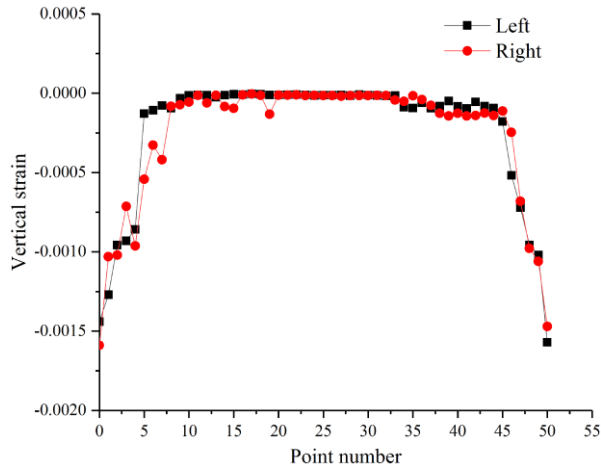
(b) Vertical strain of the measuring lines on the left- and right-sides at the end point
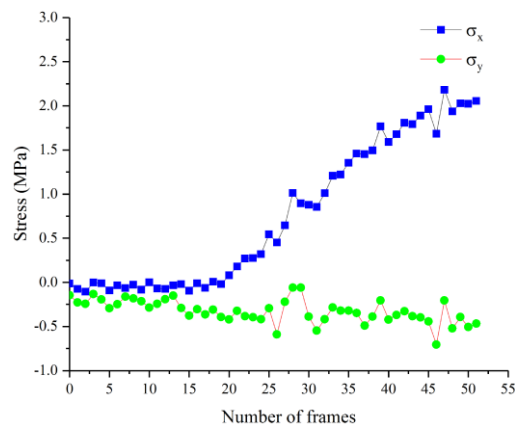
Fig. 12 – Horizontal and vertical strains of the measuring lines

The horizontal strain data of the top and bottom measured points were input in Equation 13, while the vertical strain data of measured points at the loading end were input in Equation 14. The following results were obtained based on calculations: $\varepsilon_{ha} = 0$, $\varepsilon_{ea} = 0$, $e_{hb} = 1.008 \times 10^{-3}$, and $e_{eb} = 2.467 \times 10^{-4}$. The stress value at the beginning and end of the deformation stage was determined based on the time correspondence. The above estimated data were input in Equations 15 and 16. The following results were obtained based on calculations: $E_{av} = 1580$ MPa and $\mu_{av} = 0.24$.
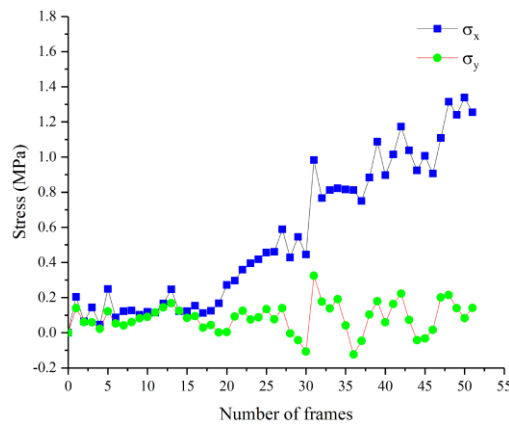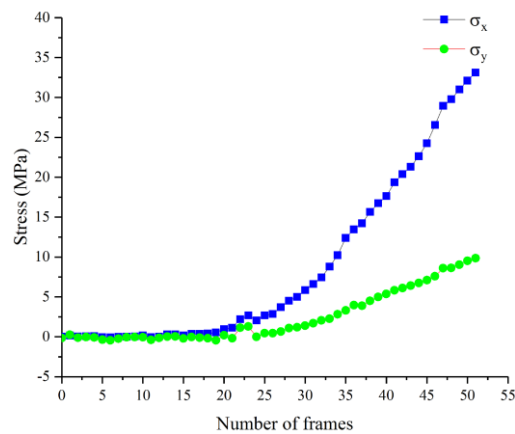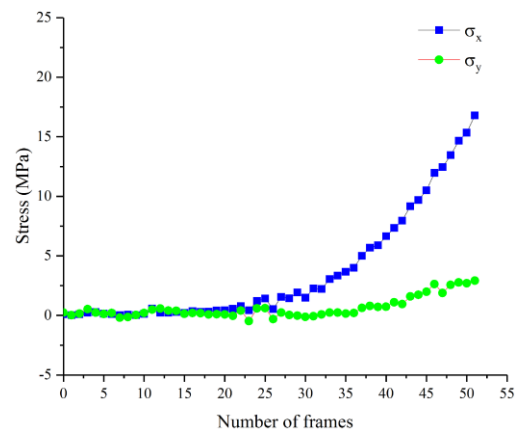

(a) Stress at point 1

Fig. 13 – Horizontal and vertical stress plots as a function of the number of frames

(b) Stress at point 2

(c) Stress at point

(d) Stress at point 4

Fig. 13 – Horizontal and vertical stress plots as a function of the number of frames

The horizontal and vertical stresses can be obtained by using the four points in Figure 8 as the concerned points for stress reconstruction and by inputting the horizontal and vertical strains and the calculated elastic modulus and Poisson's ratio in the deformation process in Equations 8 and 9 (Figure 13). The positive and negative values represent only the stress direction and not the value. As shown in Figure 13, the horizontal stress of the four points increased significantly compared with the vertical stress, indicating that the horizontal stress primarily affects the

specimen. In addition, by comparing the horizontal stresses at different points, it can be observed that the point order (from large to small stress values) is 3, 4, 2, and 1. In particular, the stress at point 3 is slightly greater than that at point 4 and far greater than those at points 1 and 2. Therefore, point 3 is the first crack point with the highest strain and stress concentration.

Therefore, the results of stress reconstruction are consistent with the macro phenomenon and DSM that verifies the feasibility of stress reconstruction for the analysis of the stress change law of the OGFC.

CONCLUSION

(1)   During the four-point bending test of the OGFC, we observed a strain concentration zone in the horizontal strain field at the mortar distribution until a crack occurred at the highest strain concentration.

(2)   The quantitative analysis of the strain of the concerned points showed that the strain increased nonlinearly, and the growth was initially slow, then accelerated, and then tended to be linear. Strain responses were disrupted owing to the cracking of the specimen at the strain concentration zone and tended to be stable at a later stage in the noncracking zone.

(3)   The stress–strain inversion and stress reconstruction of the DSM confirm that the stress reconstruction is effective and feasible for the analysis of the stress variation law of the OGFC.

ACKNOWLEDGEMENTS

REFERENCES

[1]   Qun Y., Guo Z.Y., 2005. Mixture Design of Fire-Retarded OGFC in Road Tunnel. Road Materials and Pavement design, vol. 6(2): 255-268.

[2]   Xiong R., Fang J.H., Xu A.H., Guan B.W., Liu Z.Z., 2015. Laboratory Investigation on the Brucite Fiber Reinforced Asphalt Binder and Asphalt Concrete. Construction and building materials, vol. 83: 44-52.

[3]   Tanzadeh R., Tanzadeh J., Honarmand M., Tahami S.A. , 2019. Experimental Study on the Effect of Basalt and Glass Fibers on Behavior of Open-graded Friction Course Asphalt Modified with Nano-silica. Construction and building materials, vol. 212:467-475.

[4]   Lee L., Charles R., Nicola S., 2016. Stress-Strain Behaviour of Asphalt Concrete in Compression. Procedia structural integrity, vol. 2: 2913-2920.

[5]   Pirmohammad S., Shokorlou Y.M., Amani B., 2020. Laboratory Investigations on Fracture Resistance of Asphalt Concretes Reinforced with Carbon and Kenaf Fibers at -15 degrees. Engineering fracture mechanics. vol. 230: 1-19.

[6]   Ahmad M; Bairgi B.K.; Khan Z.H.; Tarefder R.A., 2020. Evaluation of the Fracture Resistance of Asphalt Concrete Mixes Including the Effect of Anisotropy. International journal of pavement research and technology, vol. 13(2): 121-128.

[7]   Xu H.N., et al., 2019. Investigation of Anisotropic Flow in Asphalt Mixtures Using the X-ray Image Technique: Pore Structure Effect. Road materials and pavement design, vol. 20(3): 491-508.

[8]   Huang Y.H., Liu L., Sham F.C., et al., 2010. Optical Strain Gauge vs. Traditional Strain Gauges for Concrete Elasticity Modulus Determination. Optik, vol. 121(18):1635-1641.

[9]   Maas H., Hampel U., 2006. Photogrammetric techniques in civil engineering material testing and structure monitoring. Photogrammetric Engineering and Remote Sensing, vol. 72:39-45.

[10]   Kovačič B., Kamnik R., Premrov M., Gubeljak N., Predan J., Tišma Z.,2008. Modern deformation measurement techniques and their comparison. Strojniški vestnik, vol. 54:364-371.

[11]   Stewart C.M., Garcia E., 2018. Fatigue Crack Growth of a Hot Mix Asphalt Using Digital Image Correlation. International journal of fatigue, vol. 120: 254-266.

[12]   Birgisson B., et al., 2009. An Optical Strain Measurement System for Asphalt Mixtures. Materials and structures, vol. 42(4): 427-441.

[13]   Teo, T.,2020. 3D deformation measurement of concrete wall using close-range photogrammetry. ISPRS - International Archives of the Photogrammetry, Remote Sensing and Spatial Information Sciences, vol. 43:1175-1179.

[14]   Lyons J.S., Liu J., Sutton M.A., 1996. High-temperature Deformation Measurements Using Digital-Image Correlation. Experimental mechanics, vol. 36(1): 64-70.

[15]   Hu, Y., Wang, S., Cheng, X., Xu, C., Hao, Q., 2020. Dynamic Deformation Measurement of Specular Surface with Deflectometry and Speckle Digital Image Correlation. Sensors (Basel, Switzerland), vol. 20(5):1278.

[16]   Lu H., Cary P.D., 2000. Deformation Measurements by Digital Image Correlation: Implementation of a Second-order Displacement Gradient. Experimental mechanics, vol. 40(4): 393-400.

[17]   Šedina J., Pavelka K., Housarová E.,2016. Using of photogrammetric methods for deformation measurements and shape analysis. The 2nd International Conference on Engineering Sciences and Technologies, vol. 2016:859-864.

[18]   Yuan Y., et al., 2014. Accurate Displacement Measurement via a Self-adaptive Digital Image Correlation Method based on a Weighted ZNSSD Criterion. Optics and lasers in engineering, vol. 52: 75-85.

[19]   Li C., Wang L., Xiao-xiao W., 2017. Crack and Crack Growth Behavior Analysis of Asphalt Mixtures based on the Digital Speckle Correlation Method. Construction and building materials, vol. 147: 227-238.

[20]   Xue Q., et al., 2013. Dynamic Behavior of Asphalt Pavement Structure under Temperature-stress Coupled Loading. Applied thermal engineering, vol. 53(1): 1-7.

[21]   Underwood B.S., Kim Y.R., 2011. Experimental Investigation into the Multiscale Behaviour of Asphalt Concrete. International journal of pavement engineering. vol. 12: 357-370.

[22]   Kumar M., Gaur K.K., Shakher C., 2015. Measurement of Material Constants (Young's Modulus and Poisson's Ratio) of Polypropylene Using Digital Speckle Pattern Interferometry (DSPI). Journal of the Japanese Society for Experimental Mechanics, vol. 15 (Special_Issue): s87-s91.